SPE-206109-MS

Electrical, Diffusional, and Hydraulic Tortuosity Anisotropy Quantification Using 3D CT-Scan Image Data

Andres Gonzalez and Zoya Heidari, The University of Texas at Austin; Olivier Lopez, Equinor

Abstract

Depositional mechanisms of sediments and post-depositional process often cause spatial variation and heterogeneity in rock fabric, which can impact the directional dependency of petrophysical, electrical, and mechanical properties. Quantification of the directional dependency of the aforementioned properties is fundamental for the appropriate characterization of hydrocarbon-bearing reservoirs. Anisotropy quantification can be accomplished through numerical simulations of physical phenomena such as fluid flow, gas diffusion, and electric current conduction in porous media using multi-scale image data. Typically, the outcome of these simulations is a transport property (e.g., permeability). However, it is also possible to quantify the tortuosity of the media used as simulation domain, which is a fundamental descriptor of the microstructure of the rock. The objectives of this paper are (a) to quantify tortuosity anisotropy of porous media using multi-scale image data (i.e., whole-core CT-scan and micro-CT-scan image stacks) through simulation of electrical potential distribution, diffusion, and fluid flow, and (b) to compare electrical, diffusional, and hydraulic tortuosity.

First, we pre-process the images (i.e., CT-scan images) to remove non-rock material visual elements (e.g., core barrel). Then, we perform image analysis to identify different phases in the raw images. Then, we proceed with the numerical simulations of electric potential distribution. The simulation results are utilized as inputs for a streamline algorithm and subsequent direction-dependent electrical tortuosity estimation. Next, we conduct numerical simulation of diffusion using a random walk algorithm. The distance covered by each walker in each cartesian direction is used to compute the direction-dependent diffusional tortuosity. Finally, we conduct fluid-flow simulations to obtain the velocity distribution and compute the direction-dependent hydraulic tortuosity. The simulations are conducted in the most continuous phase of the segmented whole-core CT-scan image stacks and in the segmented pore-space of the micro-CT-scan image stacks. Finally, the direction-dependent tortuosity values obtained with each technique are employed to assess the anisotropy of the evaluated samples.

We tested the introduced workflow on dual energy whole-core CT-scan images and on smaller scale micro-CT-scan images. The whole-core CT-scan images were obtained from a siliciclastic depth interval, composed mainly by spiculites. Micro-CT-scan images we obtained from Berea Sandstone and Austin Chalk formations. We observed numerical differences in the estimates of direction-dependent electrical, diffusional, and hydraulic tortuosity for both types of image data employed. The highest numerical

differences were observed when comparing electrical and hydraulic tortuosity with diffusional tortuosity. The observed differences were significant specially in anisotropic samples.

The documented comparison provides useful insight in the selection process of techniques for estimation of tortuosity. The use of core-scale image data in the proposed workflow provides semi-continuous estimates of tortuosity and tortuosity anisotropy which is typically not attainable when using pore-scale images. Additionally, the semi-continuous nature of the tortuosity and tortuosity anisotropy estimates in whole-core CT-scan image data provides an excellent tool for the selection of core plugs coring locations.

Introduction

The depositional mechanisms of sediments and the post-depositional processes impact the spatial distribution of the rock components and the pore structure of sedimentary rocks, which consequently affect petrophysical and mechanical properties of the rock. Additionally, the spatial distribution of rock components and pore structure influence the directional dependency of various rock properties. Accurate estimation of direction-dependent properties of sedimentary rocks is necessary for reservoir geo-modeling and subsequent reservoir simulation as well as for completion decisions. Anisotropy is typically quantified by measuring the desired property at different orientations and computing the ratio of the measured property between different orientations. One of the most common examples is permeability anisotropy which is typically estimated by measuring horizontal and vertical permeability on adjacent core plugs oriented horizontally and vertically with respect to the bedding plane. Similarly, anisotropy in mechanical properties is quantified by measuring stress, deformation, compressional-wave, and shear-wave velocity in at least a horizontally and a vertically oriented core plug (Sone 2012).

Modern imaging techniques such as X-ray micro-computed tomography (micro-CT) and scanning electron microscopy (SEM) have been employed to capture the pore network of sedimentary rocks, resolving structures in the micron/nanometer scale (Rassenfoss 2011). The advent of this technology has allowed the simulation of distinct physical phenomena in porous media (pore-scale modeling) at the pore-Scale domain. Pore-scale modeling has been used to simulate fluid flow in porous media to estimate permeability and permeability anisotropy (Al Mansoori et al. 2014; Sun et al. 2014). Similarly, other transport properties such as electric conduction and gas diffusion can be simulated. In addition to the estimation of transport properties, these simulations can also be employed to estimate the tortuosity of the porous media employed as simulation domain (Fu et al. 2021). The use of simulation in digital pore networks of sedimentary rocks has been widely used to estimate transport properties and rock anisotropy. However, X-ray computed tomography scanning (CT-scanning) images acquired images do not necessarily reveal the pore structure of the rock, but they can reveal the spatial distribution of mineral rock components. Opening the possibility of estimation of rock anisotropy at the core-scale domain.

Tortuosity is a characteristic parameter of porous media that account for the sinuosity and complexity of the internal pathways of the porous media. Additionally, it commonly appears in the formulations to estimate transport properties (Clennell 1997; Ghanbarian et al. 2013; Fu et al. 2021) such as in the Carman-Kozeny equation to estimate permeability (Kozeny 1927; Carman 1937). Depending on the application, the estimated tortuosity can be in terms of electrical, diffusional, thermal, or hydraulic processes. However, the tortuosity calculated through distinct physical processes in general is not the same (Clennell 1997). Furthermore, the distinct tortuosity values are used interchangeably in the literature (Ghanbarian et al. 2013), which can lead to confusion. For instance, Chen and Heidari (2015) developed a workflow to quantify the directional connectivity of rock constituents and its effect on electrical resistivity of organic-rich mud-rocks. The workflow included the computation of directional tortuosity, which was calculated employing a random walk algorithm (Nakashima and Kamiya 2007) mimicking the physical phenomenon of diffusion. Since the purpose of the documented work was to quantify the effect of the connectivity (which includes the directional tortuosity), the use of electrical tortuosity for the computations would have been aligned with

the physical phenomenon of electrical conduction. Consequently, it is important to quantify the differences in the tortuosity values computed through simulation of various physical phenomenon.

In this paper, we document a workflow for estimation of tortuosity anisotropy in both whole-core CT-scan and micro-CT-scan image stacks and compare the tortuosity estimates obtained from simulation of electric potential distribution, diffusion, and fluid flow in porous media. First, we pre-processed the whole-core CT-scan image stacks to eliminate undesired non-core material portions in the raw image slices. Then, we segmented the visually identifiable phases of the whole-core CT-scan image stacks employing a supervised learning algorithm. The employed micro-CT-scan images were already segmented and pre-processed. Afterwards, we conducted simulation of electric potential distribution, diffusion, and fluid flow to obtain electrical, diffusional, and hydraulic tortuosity in all three cartesian directions. Simulations were conducted for both whole-core CT-scan (in the most continuous phase) and micro-CT-scan (in the pore space) image stacks.

Method

We introduced a workflow for estimation of direction-dependent tortuosity and anisotropy assessment through numerical simulation of hydraulic, diffusional, and electrical transport processes using segmented image stacks from whole-core CT-scan images and micro-CT-scan images. Fig. 1 illustrates the proposed workflow.
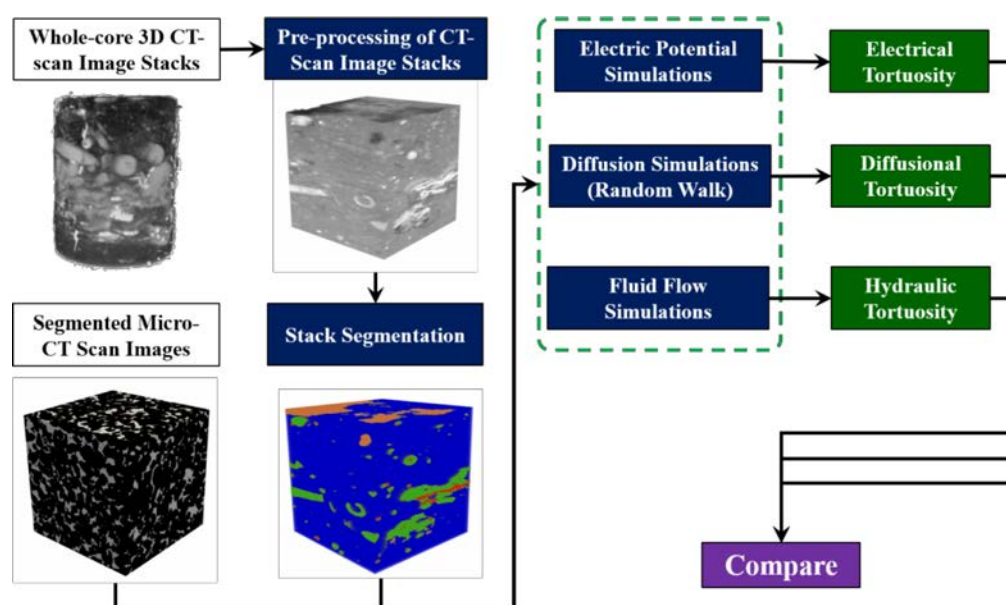

Figure 1—Workflow for estimation of direction-dependent tortuosity and rock anisotropy.

The proposed workflow includes pre-processing and image segmentation of the visually identifiable phases of the whole-core CT-scan image stacks, numerical simulation of electric potential distribution, diffusion, and fluid flow in both segmented whole-core CT-scan and micro-CT-scan image stacks, and estimation of direction-dependent tortuosity by means of numerical simulations of physical processes. Rock anisotropy calculation through tortuosity estimates and comparison of tortuosity estimates obtained via the simulation of the aforementioned physical phenomena. Pre-processing and segmentation of micro-CT-scan images was not conducted in this work, since segmented image stacks were available.

Pre-processing of Whole-core CT-scan Image Stacks
Acquisition of the employed whole-core CT-scan image stacks is typically accomplished with the core material (e.g., sandstone) contained in the core barrel used in the coring process. As such, the raw image

stacks contain visual elements that do not correspond to the core material. Examples of non-core material visual elements are the core barrel used in the coring process and gypsum employed to stabilize the core material during the coring process. Fig. 2a shows an example of a raw image slice, displaying the core material, the core barrel, and gypsum. Removal of the non-core material visual elements is necessary to conduct the subsequent steps of the proposed workflow. The core barrel is displayed as a circular ring surrounding the core material. Gypsum appears as a bright material between the core barrel and the core material. To remove the non-core material visual elements, first we employed an edge detection technique (Canny 1986) to identify the edges of each whole-core CT-scan image slice. Then, we use the detected edges as an input for a parametric curve detection technique, the Hough transform (Hough 1962). The outputs of the Hough transform are the parameters of the curve that best fit the detected edges. In this case, our objective was to identify the circumference formed by the core material. We condensed the search space by limiting the potential circumference radii to the size of the retrieved core (i.e., 4 inches outside diameter). Once we obtained the best fitting circumference, we replaced the value of all the pixels outside of the detected circumference with a characteristic value and were not utilized for further analysis. Fig. 2 shows all the steps of the workflow to remove the non-core material elements from the raw whole-core CT-scan image stacks. Finally, to conduct our simulations in a cartesian coordinate system we cut a rectangular prism from the cylinder obtained in the previous step. We fitted the largest possible square within the perimeter of the circumference of each whole-core CT-scan slice (red line in Fig 2c).
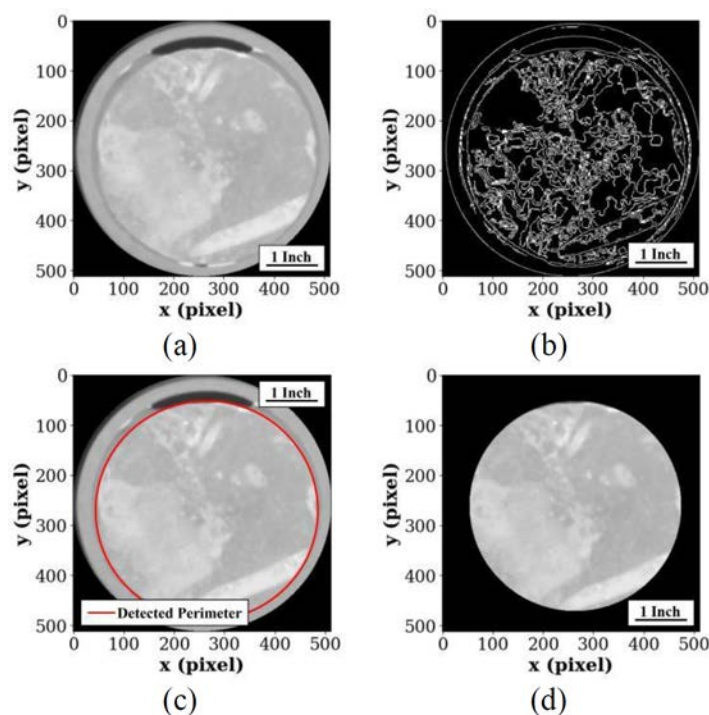
Figure 2—An example for the process of removing non-core material visual elements: (a) raw CT-scan image slice, (b) detected edges, (c) detected core perimeter, and (d) processed CT-scan image slice.

Segmentation of Whole-core CT-scan Image Stacks

The numerical simulations are conducted in the most continuous phase in the case of the whole-core CT-scan image stacks and in the pore space in the cases of micro-CT-scan image stacks. For this purpose, we used the WEKA 3D trainable segmentation plug-in (Arganda-Carreras et al. 2017) accessible in the image analysis software ImageJ-Fiji (Schindelin et al. 2002). The segmentation scheme used in WEKA 3D relies in the extraction of image-based features and a supervised learning algorithm. First, we manually selected regions of the image representing each one of the visually identifiable phases in several whole-core CT-

scan image slices. The selected regions are the inputs for the WEKA 3D algorithm, which calculates the mean and variance of each selected region and uses those estimates to train a Random Forest algorithm (Ho 1995). Finally, we used the trained algorithm to segment the full image stack (rectangular prism). Fig. 3 presents an example of the selected regions of interest for the visually identifiable phases and the segmented image slice. The red, green, and yellow phases represent rock constituents with increasing density from red to green to yellow.
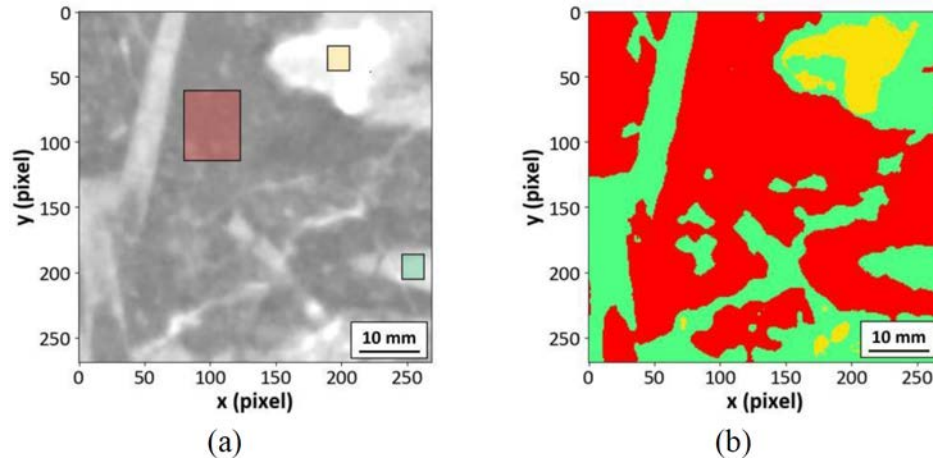

Figure 3—An example for the CT-scan image slice segmentation process: (a) CT-scan image slice and (b) segmented CT-scan image slice. The colored rectangles show examples of the visually identified phases.

Tortuosity Estimation

We used the segmented whole-core CT-scan and micro-CT-scan image stacks as the domain for the simulation of electric potential distribution, diffusion, and fluid flow through porous media. As previously mentioned, simulations are conducted in the most continuous solid phase of the whole-core CT-scan image stacks and in the pore space of the micro-CT-scan image stacks. In the case of whole-core CT-scan image stacks, we assumed that the most continuous phase is electrically conductive for the case of electrical conductivity simulations. The same phase is considered as space available for fluid flow and diffusion in the cases of fluid flow and diffusion simulations. In the following sections, we explain the method employed to conduct each one of the aforementioned simulations.

Electrical tortuosity.   To compute the electrical tortuosity, we first estimated the electric potential distribution of the segmented samples. Then, we estimated the current density and the distance covered by each electric charge after applying a potential difference using a streamline algorithm. Finally, we used the computed lengths to estimate electrical tortuosity.

We estimated the electric potential distribution in the segmented whole-core CT-scan and micro-CT-scan image stacks by solving the steady-state continuity equation for electric charges defined as

$$\nabla \cdot (J) = \nabla \times (\sigma \nabla E) = 0, \tag{1}$$

where σ is the electric conductivity, E is the electric potential, and J is the electric current density. First, we discretized the simulation domain employing a cartesian framework. Afterwards, we solved Equation 1 utilizing the transmissibility method (Garcia and Heidari 2018) by computing the half-cell transmissibility defined in the x direction as

$$T_x = 2\sigma_x \frac{\Delta_y \Delta_z}{\Delta_x}, \tag{2}$$

where Δx, Δy, and Δz are the dimensions of the grid cells in each cartesian direction. We computed the electrical transmissibility in the y and z directions in an analogous fashion. To conduct the simulations in

each cartesian direction, we applied boundary conditions of a constant electric potential difference in the two faces perpendicular to the direction of interest and no potential difference in the remaining faces of the cubic domain. The problem is reduced to an algebraic linear problem and we solved it employing the biconjugate gradient technique (Barrett et al. 1994).

After solving for the electric potential distribution in each cartesian direction, we estimated the electric current density as

$$J = \sigma \nabla E, \tag{3}$$

Where σ is the electrical conductivity of the phase available for electrical current flow, and E is the electric potential distribution in each cartesian direction. Then, we employed the electrical current density as an input for a streamline tracing algorithm. The algorithm we employed is described in the publication by Pollock (1988). The algorithm was developed for tracing particles in ground water flow modeling. The method employs the velocity distribution to track the path of individual particles using semi-analytical equations. However, in this paper we used the electric current density as suggested by Garcia and Heidari (2018) instead of particle velocity. The electric current density is related to the drift velocity in the x-direction via

$$J_z = J_{11} + (J_{12} \quad J_{11})\frac{x}{\Delta_x}, \tag{4}$$

We computed the drift velocity in each cartesian direction. Then, we used the computed drift velocities to estimate the hypothetic time that would take for a charge to travel from one end to the other end of the grid cell in each cartesian direction. Afterwards, the lowest time estimated is employed to determine the direction in which the charge is leaving the cell. The calculations are repeated for every particle in the domain. The outcome is a set of streamlines describing the path of each charge when traveling from the face of the highest electric potential to the face of the lowest electric potential of the cubic domain. Finally, we computed the electrical tortuosity via

$$\tau_{e,i} = \sum_{s=1}^{ns} \frac{L_{s,i}}{L}, \tag{5}$$

Where Ls,i is the length of the streamline of each particle in the i-th direction, ns is the total number of streamlines, and L is the length of the sample in the i-th direction, which is the direction in which the electric potential difference is applied.

Diffusional Tortuosity.   To compute the diffusional tortuosity, we simulated the process of gas diffusion employing a random walk algorithm. For this purpose, we employed Pytrax (Tranter et al. 2019) a readily available open-source Python library. The required inputs for tortuosity estimation using the Pytrax library are the simulation domain identifying the space available for diffusion and the space where no diffusion is possible, the number of walkers, and the number of time steps of the simulation. The use of a random-walk algorithm in the Pytrax library is aimed to simulate Brownian motion which can be compared to diffusive flow. Then, the tortuosity is computed as the ratio of the diffusivity in free space to the diffusivity in the restricted simulation domain. The mean square displacement (MSD) of a simple walk and equal probability of movement in each direction, is defined by a Gaussian distribution. Then, the probability of the location x of a walker at a time t can be computed via

$$p(x, t) = \frac{1}{\sqrt{4\pi D t}} \exp\left(\frac{x2}{4Dt}\right), \tag{6}$$

where D is the diffusion coefficient. The N-dimensional mean square displacement is defined as

$$E(R_t^2) = \int_{\infty}^{\infty} (x_1^2 + \cdots + x_N^2) p(x, t) dx_1 \cdots dx_N = 2NDt, \tag{7}$$

Consequently, the MSD is the sum of the contribution of displacement in each direction. Then, the N-axial square displacements (ASD) are computed via

$$E(x_{i,t}^2) = \int_\infty^\infty x_i^2 p(x, t) dx = 2D_i t,$$
(8)

Finally, the tortuosity in each cartesian direction, i, is computed via

$$\tau_{d,i} = \frac{t}{N} \frac{1}{E(x_{i,t}^2)},$$
(9)

The assumptions of the algorithm code in the Pytrax library include: (a) the walkers do not enter to the solid phase (space where no diffusion possible), (b) the walkers move only in orthogonal direction (i.e., no diagonal displacement is allowed), (c) a walker reaching the solid phase will not keep moving, instead it will bounce back to its original position, (d) when a walker reaches the boundary of the simulation domain it is not contained, instead it keeps moving in mirror copies of the simulation domain to prevent overestimation of the tortuosity values, and (e) the axial squared displacement is plotted against time and a regression line is fitted and forced to have an intercept of zero, then the square root of the inverse of the slope of the regression lines is the directional tortuosity.

Hydraulic tortuosity.   To estimate hydraulic tortuosity, we simulated the process of fluid flow in porous media using Palabos (Palabos 2021) an open-source Lattice Boltzmann Method (LBM) solver. The required inputs include a stack of two-dimensional (2D) images that define the space available for fluid flow, the rock matrix, the rock matrix boundaries in contact with the fluid, the dimensions of the sample in all cartesian directions, and the applied pressure drop across the desired direction in lattice units.

Palabos aims to solve the Boltzmann transport equation defined as

$$\frac{\delta f}{\delta t} + \frac{\delta f}{\delta r} v + \frac{\delta f}{\delta v} a = \Omega,$$
(10)

where f is the distribution function which is a function of r (position), v (velocity), and t (time), and Ω is the collision operator. In our simulations, we used the Bhatnagar-Gross-Krook (BGK) collision operator defined as

$$\Omega = \frac{f \quad f^{eq}}{\tau_t},$$
(11)

where τt is the relaxation time and feq is the Maxwell-Boltzmann distribution computed via

$$f^{eq} = \rho \left(\frac{m}{2\pi kT}\right)^{\frac{D_m}{2}} \exp\left(\frac{m(v \quad u)^2}{2kT}\right),$$
(12)

where ρ, u, and T are the density, the velocity, and the temperature of the fluid, k is the Boltzmann constant, m is the mass of the molecules, and Dm is the spatial dimension the molecules move in. In our simulation we used D3Q19 lattice. The output of the fluid flow simulations includes the velocity distribution in the simulation domain, which can be employed to estimate the permeability of the media. However, we are not interested in the permeability of the media, but in the direction-dependent tortuosity. For that purpose, we computed the direction-dependent tortuosity defined by Matkya and Koza (2012) as

$$\tau_{h,i} = \frac{\sum_{r=1}^{n} u(r)}{\sum_{r=1}^{n} u_i(r)},$$
(12)

Where $u(r)$ is the velocity magnitude, $ui(r)$ is the velocity in the i-th direction (i.e., x, y, and z), and n is the total number of cells in the cartesian simulation domain, the i-the direction corresponds to the direction in which the pressure drop is applied.

Results

Whole-core CT-scan Image Stacks

Description of the data set. We estimated direction-dependent electrical, diffusional, and hydraulic tortuosity on two dual-energy CT-scan image stacks from a siliciclastic depth interval covering approximately two meters. Fig. 4 shows the initial formation evaluation for depth interval containing the two-meter whole-core CT-scan image stack. Porosity in the evaluated depth interval ranges between 14.2% to 26.4%, while permeability ranges between 3.55 md to 268 md. The blue-shaded box indicates the location of the employed whole-core CT-scan image stacks. The main lithology of the selected depth intervals includes spiculites, a biogenic sedimentary rock composed by sponge silica spicules. The resolution of the employed whole-core CT-scan image stacks is 0.234 mm/pixel in the *x*- and *y*- directions and 0.5 mm/pixel in the *z*-direction. However, we rescaled the resolution of the image stacks in the *x*- and *y*- directions to match the resolution in the *z*-direction to preserve a homogeneous discretization of the simulation domain. Fig. 5 shows three-dimensional (3D) renders of whole-core CT-scan image stacks
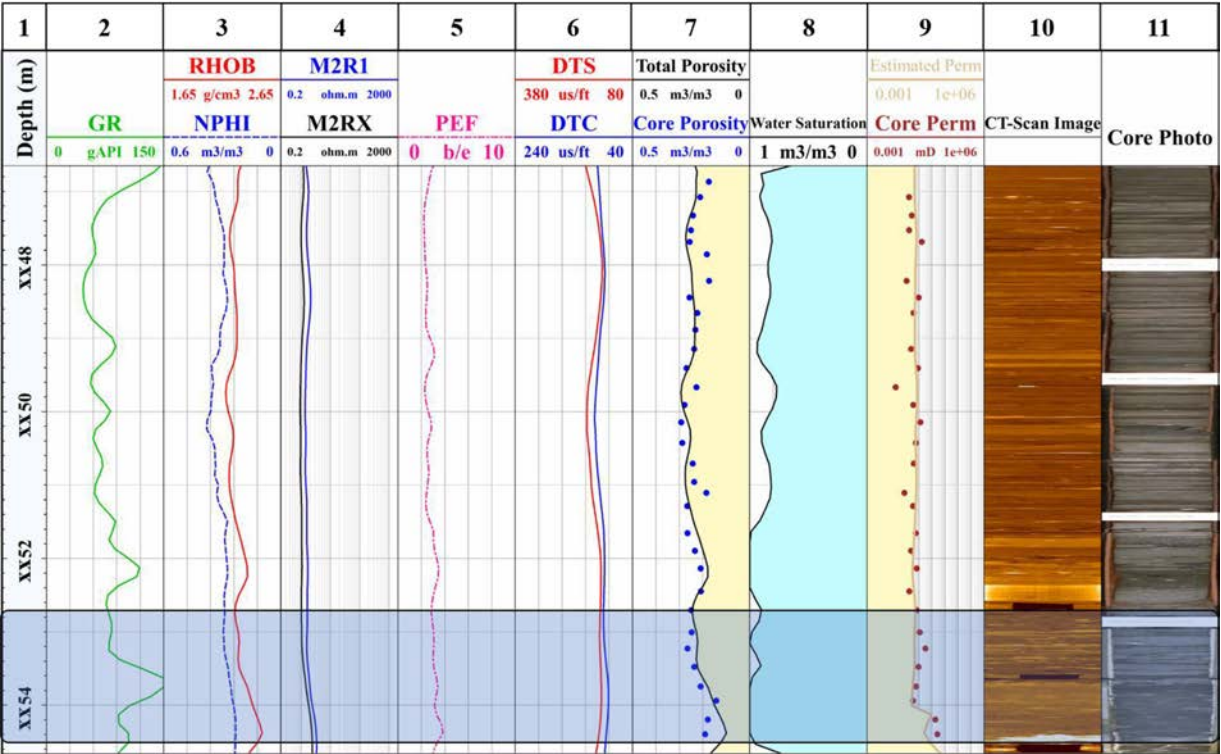

Figure 4—Conventional formation evaluation - Tracks from left to right: track 1: depth; track 2: gamma-ray (GR); track 3: bulk density (RHOB) and neutron porosity (NPHI, in water-filled sandstone units); tracks 4: shallow (M2R1) and deep resistivity (M2RX); track 5: photoelectric factor (PEF); track 6: shear-wave slowness (DTS) and compressional-wave slowness (DTC); track 7: estimated total porosity and core porosity measurements; track 8: water saturation; track 9: estimated permeability and core permeability; track 10: core CT-scan image; track 11: core photo

Sample No. 1 (5a) and Sample No. 2 (5b) with raw dimensions of 512×512×1778 and 512×512×2025 (*x*-, *y*-, and *z*-direction, respectively) voxels, respectively. The final dimensions of the samples after rescaling are 126×126×1778 and 126×126×2025 voxels for Sample No. 1 and Sample No. 2, respectively. To conduct the simulations described in the method section, we partitioned the samples into cubic subsamples of 126×126×126 voxels, resulting in 14 and 16 subsamples for Sample No. 1 and Sample No. 2, respectively.

Segmentation results. In the case of whole-core CT-scan image stacks, we segmented the samples in four visually identifiable phases. We identified each phase based mainly on grey-scale differences. As explained

in the method section, we selected regions representative of each phase for image-based feature extraction and the training of the Random Forest algorithm. We trained the algorithm individually for each sample and then used the trained algorithm to segment the full stack. Fig. 6 shows the segmented phases of Subsample 12 from Sample No. 1. We labeled the most continues phase as Phase A. This is the phase that we used for numerical simulations in the whole-core CT-scan image stacks. The distribution of the remaining phases (i.e., B, C, and D) displays heterogeneity in the spatial distribution of the segmented phases despite the apparent continuity of Phase A, which can lead to rock anisotropy. We observed several subsamples with heterogeneous distribution of the segmented phases in both Sample No. 1 and Sample No. 2.
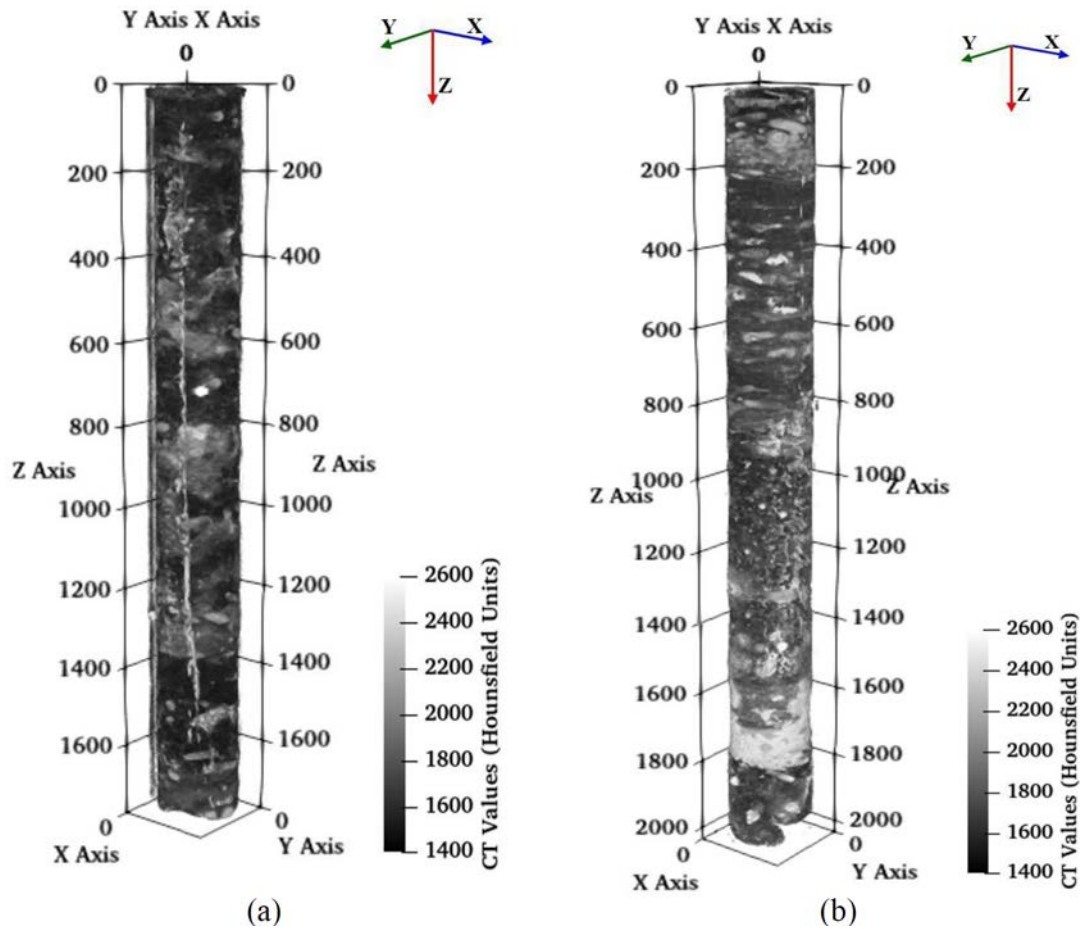

Figure 5—3D renders of whole-core CT-scan image stacks samples:
(a) Sample No. 1 and (b) Sample No. 2. (Gonzalez et al. 2021)

**Figure 6—3D renders of the segmentation results of Subsample No. 12
from Sample No. 1: (a) Phase A (b) Phase B, (c) Phase C, and (d) phase D.**

Tortuosity anisotropy estimation.   We conducted numerical simulations of all the physical phenomena documented in the method section. For this purpose, we divided the segmented whole-core CT-scan image stacks in cubic subsamples and used them as the simulation domain. We conducted all the simulations in the most continuous phase, Phase A. Numerical simulations in the most continuous phase were conducted to quantify its spatial distribution. In the case of electric potential distribution modeling, we established a potential difference of 100 volts across opposing faces of the cubic domain in the desired cartesian direction. In the random walk simulations, we used 10000 walkers and 1e7 time steps. We used 1e7 time steps to guarantee that the walkers move through the entire sample, this was checked by running random walk simulations for increasing number of time steps until the obtained tortuosity values converged to a constant value. Finally, in the fluid-flow simulations we stablished a 5e-5 pressure drop in lattice in opposing faces of the cubic domain in the desired cartesian direction. The pressure value employed was selected to ensure laminar flow regime in the simulations. We used the same simulation parameters for all the simulations in all subsamples from Sample No. 1 and Sample No. 2.

Fig. 7 shows the tortuosity estimates for all subsamples in Sample No. 1 in all three cartesian directions. In the case of the electric potential distribution, the displayed values correspond to the average electrical tortuosity computed over all generated streamlines. In the other two cases, a single value is obtained for diffusional and hydraulic tortuosity directly from the simulation results. Additionally, an unwrapped CT-scan image and a photo of the slabbed whole-core are displayed. The black-dashed line number 1 indicates an isotropic interval where the tortuosity computed for Phase A in all three cartesian directions shows similar values for all the simulated physical phenomena. On the other hand, the black-dashed line number 4 shows an anisotropic interval where the tortuosity computed for Phase A in the *z*-direction differs from the tortuosity values in both *x*- and *y*-directions, for all the simulated physical phenomena. The blue-dashed lines number 2 and 3 indicates an interval where Phase A is discontinuous in the *z*-direction. Therefore, it is expected that no tortuosity value is computed in this interval since the simulated phenomena will not occur

across the sample (i.e., from one face to the opposing face of the cubic domain). In the case of electrical tortuosity and diffusional tortuosity, we obtained the aforementioned expected behavior. In the case of the diffusional tortuosity, however, we obtained a numerical value. Nevertheless, the fitting of the line in the axial displacement against time steps results in a negative coefficient of determination, suggesting that the computed tortuosity value is not valid. In the case of hydraulic tortuosity, we also obtained a numerical value. This is a consequence of how the tortuosity is computed. The hydraulic tortuosity, the fluid-flow simulations still provide a velocity distribution array (with negligible values) and since the tortuosity is computed using Equation 12 it stills provides a numerical outcome. Track 4 of Fig. 7 shows image-based rock classes obtained from image features from CT-scan images and the use of a cluster validation index (Gonzalez et al. 2020). The obtained rock classes show a degree of agreement with the variation of the estimated tortuosity values in the *z*-direction. However, we do not expect to see a perfect correlation as the image-based features capture only the spatial distribution of the rock constituents in the plane represented by the 2D CT-scan image.
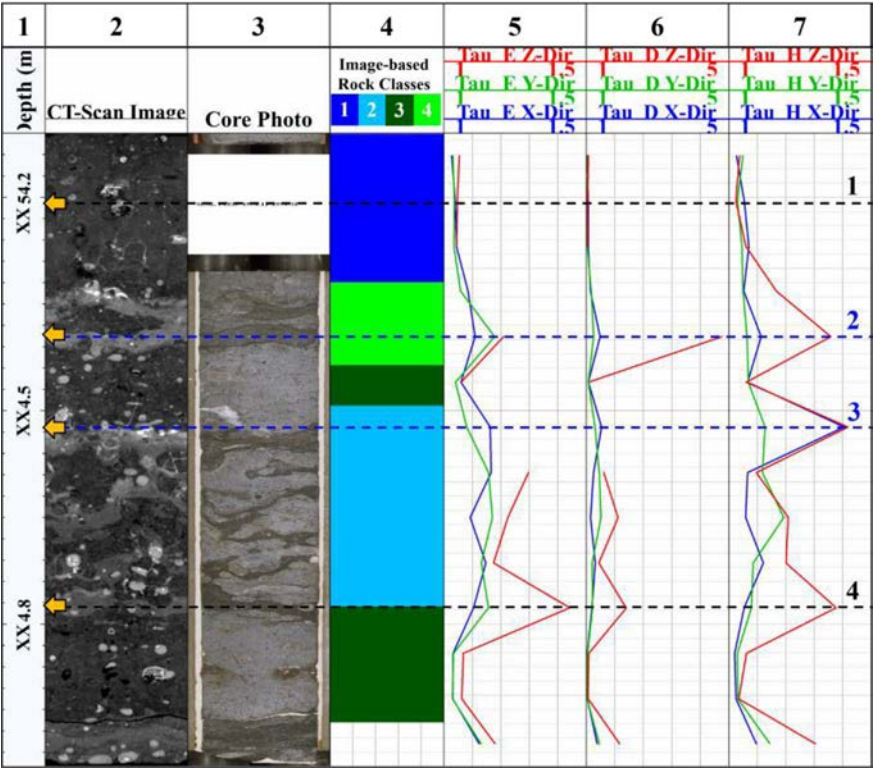

Figure 7—Sample No. 1: Tortuosity estimation. Tracks from left to right: track 1: depth; track 2: unwrapped 2D CT-scan image; track 3: slabbed whole-core photo; track 4: image-based rock classes; track 5: electrical tortuosity in the *x*- (blue), *y*- (green), and *z*-direction (red); track 6: diffusional tortuosity in the *x*- (blue), *y*-(green), and *z*-direction (red); track 7: hydraulic tortuosity in the *x*- (blue), *y*- (green), and *z*-direction (red). The black-dashed lines 1 and 4 indicate an isotropic interval and an anisotropic interval, respectively. The blue-dashed lines 2 and 3 indicates an interval where the most continuous phase is disconnected in the *z*-direction.

Fig. 8 shows the tortuosity estimates for all subsamples in Sample No. 2 in all three cartesian directions, along with an unwrapped CT-scan image and a photo of the slabbed whole-core. The tortuosity values obtained through the introduced simulation techniques show an overall isotropic depth interval, except for the first 10-15 centimeters of the retrieved core. Visual analysis of the slabbed whole-core photo and the unwrapped CT-scan image display a more visually homogeneous distribution of the mineral constituents making up the rock when compared with Sample No. 1. It should be noted that no tortuosity values are computed on the lower part of the interval due to severe loss of continuity of Phase A. Track 4 in Fig. 8 shows the image-based rock classes for the evaluated interval. In this case, we do not observe a good agreement

between the tortuosity estimates and the rock classes. This lack of agreement can be explained by the fact that the image-based features employed for image-based rock classification not necessarily capture the directional nature of the spatial distribution of rock constituents. However, it should be noted that integration of tortuosity estimates, and image-based features can potentially improve the estimated rock classes.
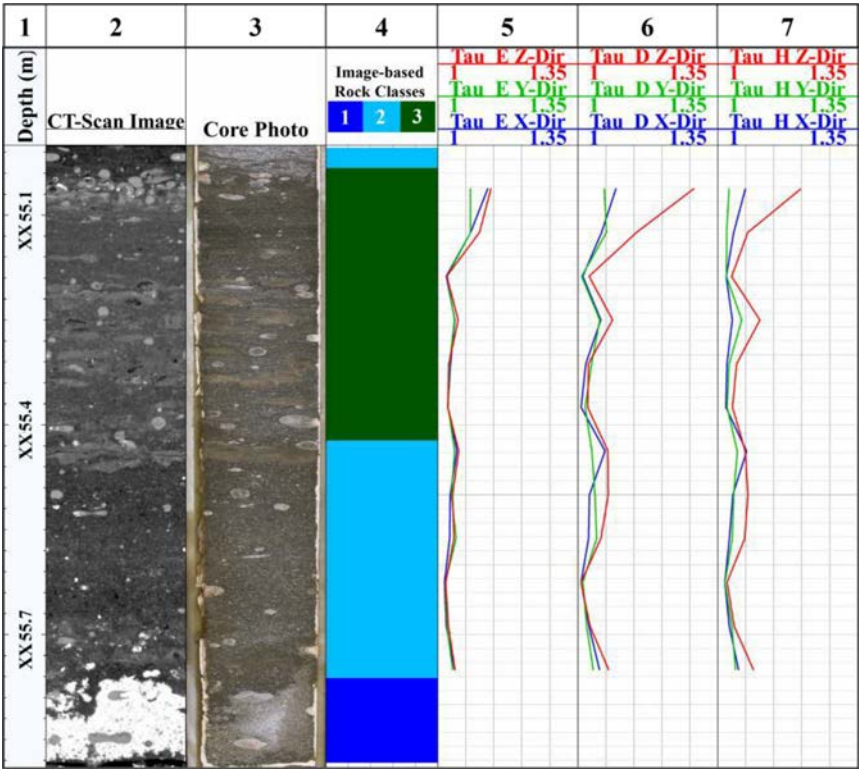

Figure 8—Sample No. 2: Tortuosity estimation. Tracks from left to right: track 1: depth; track 2: unwrapped 2D CT-scan image; track 3: slabbed whole-core photo; track 4: image-based rock classes; track 5: electrical tortuosity in the *x*- (blue), *y*- (green), and *z*-direction (red); track 6: diffusional tortuosity in the *x*- (blue), *y*-(green), and *z*-direction (red); track 7: hydraulic tortuosity in the *x*- (blue), *y*- (green), and *z*-direction (red).

The semi-continuous estimates of electrical, diffusional, and hydraulic tortuosity show a similar trend in both examples (Fig. 7 and Fig. 8) capturing the vertical variation of the evaluated depth intervals. However, measurable differences in the numerical values of the estimated tortuosity are observed, particularly in the results of Sample No.1. Figs. 9a and 9b show the mean differences between tortuosity estimates. Computed as the depth-by-depth differences in tortuosity values and averaged over the entire depth interval. The largest differences are observed between electrical and diffusional tortuosity values in the *z*-direction in both Sample No. 1 and Sample No. 2 with differences up to 0.51 and 0.03 units, respectively. The smallest differences are observed between electrical and hydraulic tortuosity with differences of 0.030 tortuosity units in the *y*-direction and between electrical and diffusional tortuosity of 0.007 tortuosity units in the *y*-direction for Sample No. 1 and Sample No. 2, respectively. The largest differences across both samples for all the conducted simulations are observed in the *z*-direction, which can be related to the increased heterogeneity in the spatial distribution of the rock components in the *z*- direction related to the depositional mechanisms of sediments.
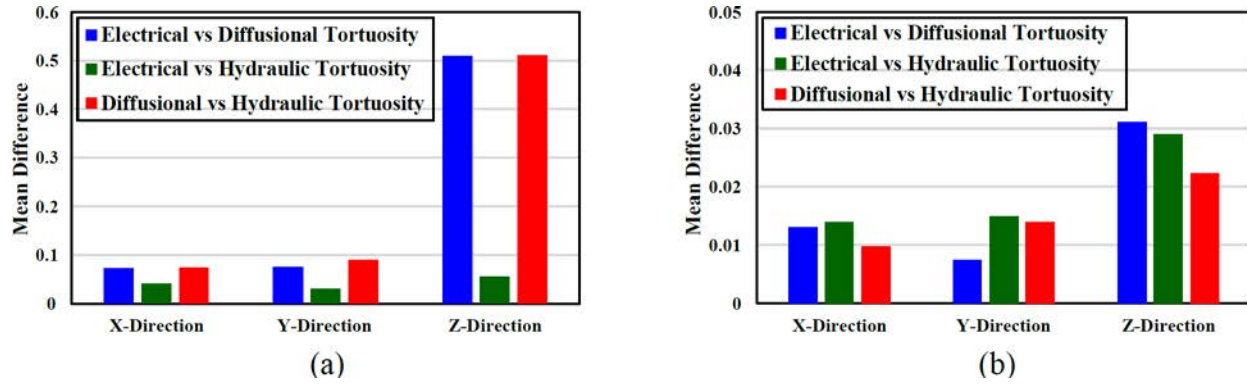
Figure 9—Mean differences between hydraulic, electric, and diffusional tortuosity estimates: (a) Sample No. 1 and (b) Sample No. 2.

Micro-CT-scan Image Stacks

Description of the data set. We conducted numerical simulations of electric potential distribution, diffusion, and fluid flow on two 3D micro-CT-scan images. The employed samples belong to two formations with different pore structure. The first image stack was acquired from a Berea sandstone sample (Dong 2007; Chi and Heidari 2016), which has a spatial resolution of 5.345 μm/pixel, porosity of 19.65%, and 400×400×400 voxels. The second image belongs to an Austin Chalk sample (Prodanovic et al. 2015; Chi and Heidari 2016), which has a spatial resolution of 0.7 μm/pixel, porosity of 29.56%, and 600×600×600 voxels. In the numerical simulations on the Austin Chalk sample, we used a 400×400×400 voxels subsample. Fig. 10 shows the 3D rendering of the segmented micro-CT-scan image stacks.
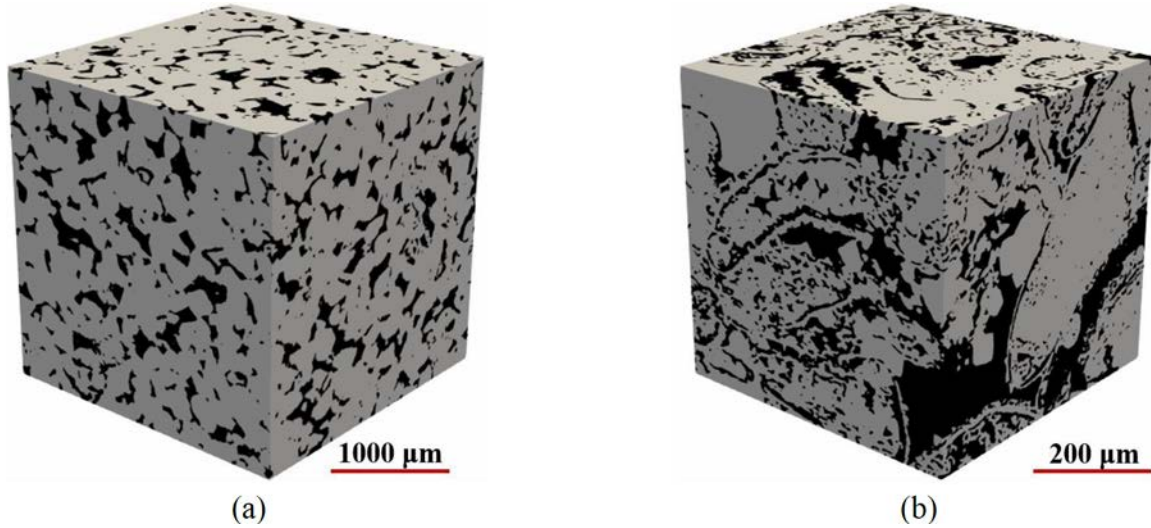

Figure 10—3D renders of segmented micro-CT-scan image stacks: (a) Berea sandstone and (b) Austin Chalk. Gray pixels and black pixels represent the grains (or matrix) and the pore space, respectively.

Tortuosity anisotropy estimation. We conducted simulations of electric potential distribution, diffusion, and fluid flow in both samples in all three cartesian directions. Simulations were conducted in the segmented pore space. In the case of electric potential distribution simulations, we assumed 100% water saturation and used a 100 volts potential difference across opposing faces of the cubic domain in the cartesian direction of interest. In the case of random walk simulations (diffusion), we used 1000 walkers and 1e7 time steps. Finally, in the case of fluid-flow simulations, we conducted single phase fluid-flow simulations with a pressure drop of 5e-5 pressure lattice units in opposing faces of the cubic domain in the direction of interest.

Fig. 11 shows tortuosity values obtained for both samples in each cartesian direction through numerical simulation of electric potential distribution, diffusion, and fluid flow. The tortuosity values obtained for the Berea sandstone segmented micro-CT-scan image (Fig. 11a) show an isotropic sample, displaying similar values of tortuosity in all three cartesian directions for electric, diffusional, hydraulic tortuosity. Comparison of electric, diffusional, and hydraulic tortuosity shows a similar behavior as observed for the results of whole-core CT-scan image stacks Sample No. 1. Hydraulic and electrical tortuosity show similar values while diffusional tortuosity shows higher values than hydraulic and electrical tortuosity. The highest observed difference between hydraulic and diffusional tortuosity in the Berea sandstone sample is 0.62 units in the x-direction tortuosity. On the other hand, the highest observed difference between electrical and diffusional tortuosity in the Berea sandstone sample is 0.76 units in the z-direction.
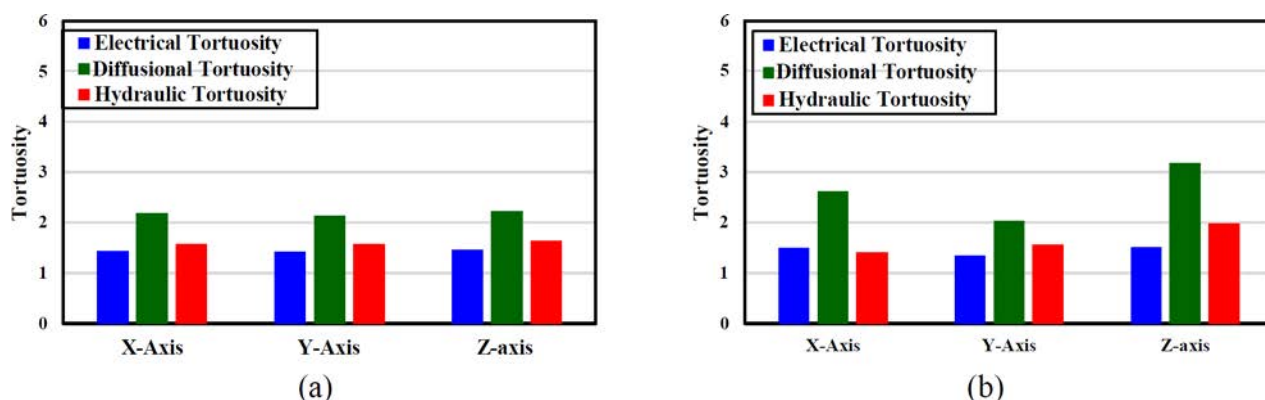

Figure 11—Electrical, diffusional, and hydraulic tortuosity estimates in segmented micro-CT-scan image stacks: (a) Berea sandstone and (b) Austin Chalk.

In the case of the Austin Chalk sample, the tortuosity values obtained (Fig. 11b) show an anisotropic sample, with measurable differences in the tortuosity values in all three cartesian directions for all three types of computed tortuosity values (electrical, diffusional, and hydraulic). Electrical and hydraulic tortuosity show similar values in the x-direction, while differences of 0.22 and 0.47 units are observed in the y- and z-direction. However, the highest differences are observed when comparing diffusional with both electrical and hydraulic tortuosity. The highest observed difference between hydraulic and diffusional tortuosity in the Austin Chalk sample is 1.21 units in the x-direction. On the other hand, the highest observed difference between electrical and diffusional tortuosity in the Austin Chalk sample is 1.66 units in the z-direction.

Conclusions

We estimated electric, diffusional, and hydraulic tortuosity in both whole-core CT-scan and micro-CT-scan image stacks. We employed the direction-dependent tortuosity estimates to assess the anisotropy of the evaluated samples. In the case of the whole-core CT-scan image stacks, the proposed method relies on the existence of at least two distinguishable phases (mineral constituents) in the raw image slices. This condition is necessary as the objective of the proposed workflow is to quantify the spatial distribution of the distinct rock constituents.

Direction-dependent tortuosity estimates correlated well with the spatial distribution of rock constituents observed in both slabbed whole-core photos and whole-core CT-scan image stacks. Additionally, results of tortuosity from simulation of electric potential distribution, diffusion, and fluid flow showed similar vertical variation in the case of whole-core CT-scan image stacks. However, measurable numerical differences were observed between the electric, hydraulic, and diffusional tortuosity estimates. The highest average differences were observed when comparing both electrical and hydraulic tortuosity values with diffusional tortuosity in Sample No. 1, with average differences in the z-direction of 0.50 and 0.51 tortuosity units,

respectively. Differences between electrical and hydraulic tortuosity are minimal for sample No. 1 in all cartesian directions. Previous publications (Clennell 1997; Ghanbarian et al. 2013) have reported that diffusional and electrical tortuosity should have similar values and that comparison of hydraulic tortuosity should display dissimilar values, which is contradictory with our findings in the case of Sample No. 1. The observed differences can be a consequence of how the tortuosity values are defined. For instance, in the work by Fu et al. (2021), electrical tortuosity is defined in two different ways, which could provide unequal tortuosity values. Additionally, differences between electrical, diffusional, and hydraulic tortuosity are expected as diffusional and electrical tortuosity are described by Laplace's equation, while hydraulic tortuosity follows the Navier-Stokes's equation (Fu et al. 2021).

In the case of pore-scale analysis, tortuosity values estimated through all the documented simulations reflected the complexity of the rock fabric for both samples. In the case of the Berea sandstone, the electrical, diffusional, and hydraulic tortuosity computed in all three cartesian direction indicated an isotropic sample. On the other hand, the electrical, diffusional, and hydraulic tortuosity values computed in each cartesian direction for the Austin Chalk indicated an anisotropic sample. Finally, we observed similar differences when compared electrical, diffusional, and hydraulic tortuosity as in the case of Sample No. 1 in whole-core CT-scan image stacks. However, the values of the numerical differences were approximately an order of magnitude higher in the case of pore-scale analysis. Tortuosity values obtained for the micro-CT-scan images were in general higher that those obtained for the whole-core CT-scan images. This observation is a consequence of the relatively higher complexity in the spatial distribution of the pore space in the micro-CT-scan images compared to the spatial distribution of the most continuous solid phase in the whole-core CT-scan images.

Additionally, we did not observe a consistent one-to-one correlation between the image-based rock classes (based on 2D image analysis) and tortuosity estimates from 3D CT-scan images. In the case of Sample No. 1, the detected rock classes had a reasonable correlation with the vertical variation in the computed tortuosity values in the z-direction. On the other hand, the detected rock classes in Sample No. 2 did not correlate well with the tortuosity values. A strong correlation is not expected as the image-based features employed for image-based rock classification are extracted on 2D images, failing to account for the three-dimensional spatial distribution of the rock components. However, integration of both image-based features and tortuosity estimates can potentially results in rock classes reflecting the 2D and 3D spatial distributions of rock components.

Disclaimer

The views and opinions expressed in this paper are those of the authors and do not necessarily reflect those of the Joint Industry Research Program members or example data owners.

Acknowledgements

Acronyms

    2D = Two-dimensional
    3D = Three-dimensional

CT   = Computed Tomography
LBM   = Lattice Boltzmann Method
MSD   = Mean Squared Distance
SEM   = Scanning Electron Microscopy
WEKA = Waikato Environment for Knowledge Analysis

Nomenclature

D = Diffusion coefficient (m2/s)
Di = Diffusion coefficient in the *i-th* direction (m2/s)
Dm = Number of dimension where the molecules are moving
E = Electric potential (Volts)
f = Distribution function
feq = Maxwell-Boltzmann distribution
$E(R_t^2)$ = N-dimensional mean square displacement (m)
$E(x_{i,t}^2)$ = N-axial square displacement (m)
J = Electric current density (A/m2)
Jz = Electric current density in the z-direction (A/m2)
k = Boltzmann constant (m2kg/s2K)
Ls,i = Length of the streamline of each particle (m)
L = length of the sample mm (m)
m = Mass of the molecules (kg)
n = Total number of cells in the cartesian simulation domain
ns = Total number of streamlines
t = time (s)
T = Temperature (K)
Tx = Electrical transmissibility (Ohm-1)
$p(x,t)$ = Probability of the location x of a walker at a time t
r = Position vector (m)
u = Macroscopic velocity vector (m/s)
$u(r)$ = Velocity magnitude (m/s)
$ui(r)$ = Velocity in the *i-th* direction
v = Velocity vector (m/s)
ρ = Density (kg/m3)
σ = Electrical conductivity (S/m)
σx = Electrical conductivity in the z-direction (S/m)
$\tau d,i$ = Diffusional tortuosity in the *i-th* direction
$\tau e,i$ = Electrical tortuosity in the *i-th* direction
$\tau h,i$ = Hydraulic tortuosity in the *i-th* direction
Ω = Collision operator

References

Al Mansoori, M., Dernaika, M., Singh, M., Al Dayyani, T., Kalam, Z., Bhakta, R., and Koronfol, S. 2014. Application of Digital and Conventional Techniques to Study the Effects of Heterogeneity on Permeability Anisotropy in a Complex Middle East Carbonate Reservoir. Presented at the Society of Petrophysicists and Well-Log Analysts 55th Annual Logging Symposium, Abu Dhabi, United Arab Emirates, 18-22 May. SPWLA-2014-VVVV.

Arganda-Carreras, I., Kaynig, V., Rueden, C., Eliceiri, K.W., Schindelin, J., Cardona, A., and Sebastian Seung, H. 2017. Trainable Weka Segmentation: A Machine Learning Tool for Microscopy Pixel Classification. *Bioinformatics* **33** (15): 2424–2426. http://dx.doi.org/10.1093/bioinformatics/btx180.

Barrett, R., Berry, M., Chan, T.F., Demmel, J., Donato, J., Dongarra, J., Eijkhout, V., Pozo, R., Romine, C., and Van der Vorst, H. 1994. Templates for the Solution of Linear Systems: Building Blocks for Iterative Methods, Second Edition. Philadelphia, Pennsylvania: Society for Industrial and Applied Mathematics (SIAM).

Canny, J. 1986. A Computational Approach to Edge Detection. *IEEE Transactions on pattern analysis and machine intelligence* **6**: 679–698, http://dx.doi.org/10.1109/TPAMI.1986.4767851.

Carman, P. C. 1937. Fluid Flow Through Granular Beds. *Trans. Inst. Chem. Eng.* **15**: 150–166.

Chen, H. and Heidari, Z. 2015. Quantifying the Directional Connectivity of Rock Constituents and its Impact on Electrical Resistivity of Organic-rich Mudrocks. *Mathematical Geosciences* **48** (3): 285–303, https://doi.org/10.1007/s11004-015-9595-9.

Clennell, M. B. 1997. Tortuosity: A Guide Through the Maze. *Geological Society*, London, Special Publications. **122** (1): 299–344. https://doi.org/10.1144/GSL.SP.1997.122.01.18.

Dong, H. 2007. Micro-CT Imaging and Pore Network Extraction. PhD thesis, Imperial College, London (December 2007).

Fu, J., Hywel R., and Chenfeng Li. 2020. Tortuosity of Porous Media: Image Analysis and Physical Simulation. *Earth-Science Reviews.* https://doi.org/10.1016/j.earscirev.2020.103439.

Garcia, A.P. and Heidari, Z. 2018. Development of a Resistivity Model that Incorporates Quantitative Directional Connectivity and Tortuosity for Enhanced Assessment of Hydrocarbon Reserves. *SPE Journal* **23** (05): 1552–1565, https://doi.org/10.2118/181571-PA.

Ghanbarian, B., Hunt, A. G., Ewing, R. P., and Sahimi, M. 2013. Tortuosity in Porous Media: A Critical Review. *Soil Science Society of America Journal* **77** (5): 1461–1477. https://doi.org/10.2136/sssaj2012.0435.

Gonzalez, A., Kanyan, L., Heidari, Z., and Lopez, O. 2020. Integrated Multiphysics Workflow for Automatic Rock Classification and Formation Evaluation Using Multiscale Image Analysis and Conventional Well Logs. *Petrophysics* **61** (05): 495–518. SPWLA-2020-v61n5a7. https://doi.org/10.30632/PJV61N5-2020a7.

Gonzalez, A., Teymouri, M., Heidari, Z., and Lopez, O. 2021. Anisotropy Quantification Using High- Resolution Whole-Core CT-Scan Images. Presented at the Society of Petrophysicists and Well-Log Analysts 62nd Annual Logging Symposium. Held online 17-20 May. SPWLA-2021-0087. https://doi.org/10.30632/SPWLA-2021-0087.

Ho, T. K. 1995. Random Decision Forests. Presented at 3rd International Conference on Document Analysis and Recognition IEEE, Montreal, Quebec, Canada, 14-16 August. https://doi.org/10.1109/ICDAR.1995.598994.

Hough, P. V. Method and Means for Recognizing Complex Patterns. U.S. Patent 3,069,654, issued December 18, 1962.

Kozeny, J. 1927. Über kapillare Leitung des Wassers im Boden-Aufstieg. *Versickerung und Anwendung auf die Bewässerung*.

Latt, J., Malaspinas, O., Kontaxakis, D., Parmigiani, A., Lagrava, D., Brogi, F., and Chopard, B. 2021. Palabos: Parallel Lattice Boltzmann Solver. *Computers & Mathematics with Applications* **81**: 334–350. https://doi.org/10.1016/j.camwa.2020.03.022.

Nakashima, Y. and Kamiya, S. 2007. Mathematica Programs for The Analysis of Three-Dimensional Pore Connectivity and Anisotropic Tortuosity of Porous Rocks Using X-ray Computed Tomography Image Data. *Journal of Nuclear Science and Technology* **44** (9): 1233–1247. https://doi.org/10.1080/18811248.2007.9711367.

Pollock, D.W. 1988. Semi-analytical Computation of Path Lines for Finite-difference Models. *Groundwater* **26** (6): 743–750.

Prodanovic, M., Esteva, M., Hanlon, M. et al. 2015. Digital Rocks Portal: A Repository for Porous Media Images, https://doi.org/10.17612/P7CC7K.

Rassenfoss, S. 2011. Digital Rocks out to Become a Core Technology." *Journal of Petroleum Technology* **63** (05): 36–41. SPE-0511-0036-JPT. https://doi.org/10.2118/0511-0036-JPT

Schindelin, J., Arganda-Carreras, I., Frise, E., Kaynig, V., Longair, M., Pietzsch, T., and Cardona, A. 2012, Fiji: An Open-source Platform for Biological-image Analysis. *Nature Methods* **9** (7): 676–682, http://dx.doi.org/10.1038/nmeth.2019.

Sone, H. 2012. Mechanical Properties of Shale Gas Reservoir Rocks, and Its Relation to the In-situ Stress Variation Observed in Shale Gas Reservoirs. *Stanford University*.

Sun, H., Vega, S., and Tao, G. 2015. Study on Permeability Anisotropy in Carbonate Reservoir Samples using Digital Rock Physics. Presented at the SPE Abu Dhabi International Petroleum Exhibition and Conference, Abu Dhabi, United Arabs Emirates, 9-12 November. SPE-177540-MS. https://doi.org/10.2118/177540-MS.

Tranter, T. G., Kok, M. D., Lam, M., and Gostick, J. T. 2019. Pytrax: A Simple and Efficient Random Walk Implementation for Calculating the Directional Tortuosity of Images. *SoftwareX* **10**: 100277. https://doi.org/10.1016/j.softx.2019.100277.